Cement and Concrete Research 124 (2019) 105810

Contents lists available at ScienceDirect

Cement and Concrete Research

journal homepage: www.elsevier.com/locate/cemconres

Binder-scale creep behavior of metakaolin-based geopolymer

Shikun Chen[a], Chenglin Wu[b], Dongming Yan[a,*]

[a] Institute of Engineering Materials, College of Civil Engineering and Architecture, Zhejiang University, Hangzhou 310058, PR China
[b] Department of Civil, Architectural, and Environmental Engineering, Missouri University of Science and Technology, Rolla, MO 65409-0030, USA

ARTICLE INFO

Keywords:
Geopolymer
Creep
Nanoindentation

ABSTRACT

In this study, the creep behavior of binder phase in metakaolin-based geopolymers (MKGs) was investigated using nanoindentation. The underlying influence of the Si/Al ratio on the creep behavior was determined from detailed microstructure characterization and micromechanical analysis. The results indicated a strong correlation between the binder-scale creep behavior in MKG and its microstructure, particularly the characteristic pore size, which was further related to the Si/Al ratios of the binder. Combined with micromechanical analysis, the underlying influence of the composition and structure on the creep behavior in MKG was further explained.

1. Introduction

Geopolymer has emerged as a potentially competitive substitute for ordinary Portland cement (OPC) in civil engineering. It can be made from a wide range of raw materials containing natural clays and industrial wastes such as fly ash, slags, or red-mud. Its processing relies on alkali-activation and subsequent polycondensation, namely geopolymerization [1–3]. This unique process provides an opportunity to satisfy the vast demand for concrete while imposing a lower environmental impact in terms of CO_2 emissions and energy consumption [4,5]. In addition, the 3D-networked molecular structure of aluminosilicate gel gives geopolymer concrete greatly improved durability and fire-resistance compared with OPC concrete [6–9]. The improved performance and reduced environmental effects make geopolymer concrete a desirable construction material for future buildings.

The creep behavior of cementitious binders significantly influences the durability and serviceability of concrete structures [10–14]. As a newly developed binder material, the creep behaviors of geopolymer have gained much attention from researchers [15–20]. Using the bulk-scale creep test, Hardjito et al. [15] showed that fly-ash-based geopolymer concrete undergoes low creep strain over 12 weeks of loading. Subsequent research has also found that the specific creep (creep strain normalized by creep stress) [19,21,22] and creep coefficient (the ratio between creep strain and elastic strain) [17,19] of fly-ash based geopolymer concrete are generally less than that of OPC concrete. Some researchers [16,21] attributed this low creep to a micro-aggregation effect of unreacted fly ash particles in the binder. However, due to the lack of a direct relationship between the binder microstructure and bulk concrete properties, the bulk creep experiment could only provide a deductive underlying explanation of the creep behavior in geopolymer. To provide small-scale direct measurements, Lee et al. [20] conducted minutes-long nanoindentation experiments to characterize the creep behavior of alkali-activated fly ash (AAFA) binder. A deconvolution analysis of the grid indentation showed that the major product of geopolymerization, the N-A-S-H gel phase, exhibited larger creep compliance while the partly-activated and non-activated phases showed smaller creep. This finding supports the previous deductions from bulk-scale results. In addition, they found that the creep behavior of individual phases would change with different composition parameters, such as the Si/Al ratio, liquid-to-solid ratio, sand-to-cement ratio, silica fume, and superplasticizer dosage. This composition dependent creep behavior of geopolymer at a small scale is consistent with findings from bulk experiments [16,18]. However, the correlation between composition and creep behavior of geopolymer remains unclear.

To this end, the composition dependent creep properties of geopolymer were investigated. Since the Si/Al ratio was found to be a determinant compositional factor of geopolymer [23–27], here it was varied to produce geopolymers with different compositions. The metakaolin-based geopolymer (MKG) is used because it is an ideal model system for geopolymers due to its high purity and reproducibility [23,25,27]. Indentation creep experiments were conducted to probe the creep behavior of geopolymer at its binder phase length scale, which would significantly exclude the influence of the large voids and defects in the bulk scale test. The results were analyzed while providing the extracted elastic modulus, hardness, and creep properties of MKGs with different Si/Al ratios. The X-ray diffraction (XRD), scanning electron microscopy (SEM), and the mercury intrusion porosimetry (MIP) measurements were gathered in parallel to characterize the chemical and

* Corresponding author.
E-mail address: dmyan@zju.edu.cn (D. Yan).

https://doi.org/10.1016/j.cemconres.2019.105810
Received 3 January 2019; Received in revised form 4 July 2019; Accepted 5 July 2019
Available online 19 July 2019
0008-8846/ © 2019 Elsevier Ltd. All rights reserved.

Table 1
Chemical composition of metakaolin powder.

Component	Al_2O_3	SiO_2	CaO	TiO_2	MgO	Na_2O	K_2O	LOI
Mass content [%]	41.64	53.29	2.78	1.04	0.43	0.27	0.21	0.34

physical structures of MKG with varying Si/Al ratios. The underlying creep mechanism in MKG with a varying Si/Al ratio and the associated relationship between composition and structural properties were determined from the experimental results and micromechanical analysis. It was found that the binder-scale creep mechanism in MKGs is dependent on the sizes of nanopores and micropores, which are determined by the Si/Al ratio.

2. Experiment

2.1. Materials

The geopolymer test sample was made from metakaolin powder and an alkali activating solution. The metakaolin (MK) powder was a commercial product called MetaMax (Basf Co.). Its chemical composition was determined using X-ray fluorescence analysis (Shimadzu-XRF-1800), the chemical composition of which is presented in Table 1. The molar ratio between the silicate and aluminate content in MK was approximately 1.08 which was close to the theoretical composition of MK (Si/Al = 1).

The alkali solution used for the chemical activation of MK powder was lab-synthesized with a commercial sodium silicate solution and sodium hydroxide pellets. The sodium silicate (SS) solution was supplied by Hengli Chem. Co., Ltd. It contained 26.0% silicate and 8.2% sodium hydroxide (equivalent oxide mass). The sodium hydroxide (NaOH, Sinopharm Chemical Reagent Co., Ltd) pellets were analytical reagents, grade 98% purity. The solutions were mixed by dissolving the appropriate amount of sodium hydroxide into a sodium silicate solution, yielding various molar ratios of SiO_2/Na_2O (modulus of silicate, Ms) ranging from 1.02 to 1.92 in solution. One solution with only sodium hydroxide and water ($SiO_2/Na_2O = 0$) was also synthesized to form the binder with the lowest Si/Al ratio (Si/Al = 1.0). These solutions were synthesized, enclosed and stored at room temperature (20 °C ± 5 °C) for 24 h to cool and stabilize the chemical species and reactivity.

2.2. Synthesis of geopolymer binder

The geopolymer binder was synthesized by mixing a desired proportion of MK powder, corresponding activating solution, and some additional water into a slurry mixture. The mix proportions yielded geopolymer binders with Si/Al ratio ranging from 1.0 to 2.1, constant Na/Al ratio (1.0), and water content (44.5%). The final mix proportion of the samples is shown in Table 2.

Synthesis was conducted with an automated mixer (ASM-DA600). The powder was gradually added into an alkali solution within 1 min while stirring. Mixing continued for another 4 min at a stirring speed of 300 rpm. The slurry was then de-aired using a 600 W ultrasonic defoamer (Cheersonic CS5000D) and cooled over ice for approximately 3 min until all macroscopic air bubbles were removed. The final mixture was poured into cylindrical plastic molds with 16 mm diameter and sealed with a plastic cap. The specimens were then placed in a curing chamber at a temperature of 60 °C and relative humidity of 90% for 24 h. The specimens were subsequently placed in the curing chamber at room temperature for continuous curing over a period of 14 d.

Table 2
Mix proportions.

	MK[g]	SS[g]	NaOH[g]	H_2O[g]	Ms	Si/Al	Na/Al	H_2O wt%
Mix 1	515.59	0	176.33	483.10	0	1.0	1.0	44.5%
Mix 2	435.11	439.85	102.70	219.82	1.02	1.6	1.0	44.5%
Mix 3	415.51	543.39	85.09	158.72	1.32	1.8	1.0	44.5%
Mix 4	319.42	512.42	55.23	81.52	1.62	1.9	1.0	44.5%
Mix 5	381.15	724.60	53.96	48.58	1.92	2.1	1.0	44.5%

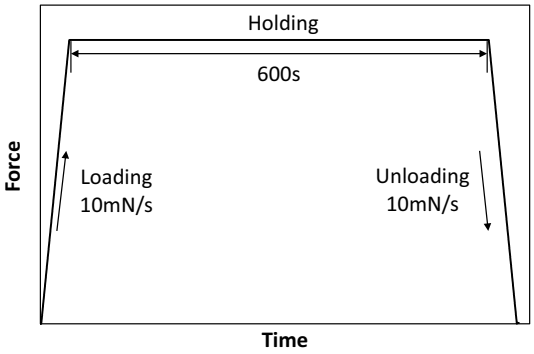

Fig. 1. Loading procedure of nanoindentation.

2.3. Nanoindentation experiments

Nanoindentation samples were cut from the cured geopolymer specimens. The samples were 8 mm tall with diameters of 16 mm. They were first embedded into an epoxy resin (EpoThin™ 2 Buehler) and then polished with silicon carbide abrasive paper (NKC waterproof) with mesh number ranging from 800# to 2000# using an automated polisher (EcoMet™300 Pro Buehler). The samples were finely polished by grinding the pre-polished surface using a diamond suspension with 0.1 μm particles for 10 min.

Nanoindentation experiments were conducted using an Agilent Nano Indenter G200 instrument equipped with a Berkovich tip. The loading procedure follows the work of El-Safty et al. [28] (Fig. 1). The indentation contains a rapid loading stage (10 mN/s), a force holding stage (last for 600 s), and a rapid unloading stage (10 mN/s). The holding force was set to 5 mN, 50 mN, 200 mN and 400 mN. However, for mix1, the indentation depth under 400 mN exceeded the test ability of the equipment and therefore only 5 mN, 50 mN and 200 mN were tested. Each experiment was initiated while the thermal drift of the system was recorded and was assured to be below 0.1 nm/s. Three or more indentations were performed at different locations for each sample.

2.4. SEM and EDS

The morphology of MKG at the micro scale was characterized using a field emission environmental scanning electronic microscope (ESEM, FEI Quanta FEG650) with an energy dispersive spectrometer (EDS, FEI EDXA 560) at 20 kV accelerating voltage. The working distance ranged from 10.5 to 12.1 mm. A point-type probe was used for energy dispersion analysis. The spectrum from each measurement point was collected over a 30 s period.

2.5. Mercury intrusion porosimetry

The pore structure of the samples was measured using mercury intrusion porosimetry (MIP) with a Micrometrics AutoPore IV 9510 instrument. The samples were cut from cylindrical specimens and crushed into coarse particles (0.9 mm to 1.2 mm). The samples were then oven-dried at 60 °C for 24 h. MIP measurements were gathered at pressures ranging from 0.5 to 60,000 psia. The evacuation pressure and time were 50 μmHg and 5 min, respectively. The mercury filling pressure was 0.5

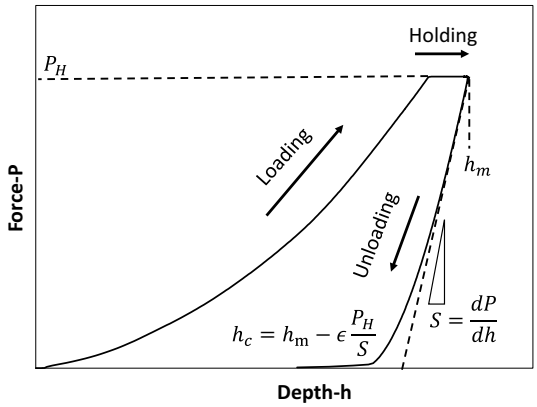

Fig. 2. Typical force–depth response of nanoindentation.

psia and the equilibration time was 10 s. Pressure was converted to pore size using the material constants of mercury (contact angle of 130°, surface tension at 485 dynes/cm, and density of 13.5335 g/mL).

3. Analysis

3.1. Hardness and Young's modulus

The typical nanoindentation response is shown in Fig. 2, which consists of three stages corresponding to three loading segments (Fig. 1). Young's modulus (E) and hardness (H) were obtained from the following equations, respectively:

$$E = (1 - \nu^2)M \tag{1}$$

$$H = \frac{P_H}{A_c} \tag{2}$$

where, ν is Poisson's ratio of the probed material, P_H is the holding force (50 mN). M and A_c are indentation modulus and contact area, respectively, and were calculated by analyzing the unloading response using the Oliver-Pharr method [29]. Detailed calculations of M and A_c are presented in Appendix A. In our previous report [30], it was shown that various Si/Al ratios caused Poisson's ratio of geopolymer, to typically range from 0.27 to 0.33. This variation is not significant. Therefore, the average Poisson's ratio (0.3) was used in further calculations.

3.2. Creep modulus and characteristic time

When indenting a viscoelastic material, the creep behavior of the probed material can be characterized using the contact creep compliance $L(t)$ [31]. For step-loaded indentation with a Berkovich tip, $L(t)$ is related to the indentation depth rate by [32] as follows:

$$\dot{L}(t) = \frac{2r_c(t)\dot{h}(t)}{P_H} \tag{3}$$

where, $r_c(t)$ is the radius of the projected area of the contact interface.

Assuming that the contact radius remains constant during the holding phase [32], the change in contact creep compliance $\Delta L(t) = L(t) - L(0)$ can be related to the change of indentation depth with time $\Delta h(t) = h(t) - h(0)$ as follows:

$$\Delta L(t) = \frac{2r_{cu}\Delta h(t)}{P_H} \tag{4}$$

where, r_{cu} is the contact radius at the end of the holding stage.

Typically, the creep in cement shows two types of behaviors: power-law [33–35] and logarithmic-law [31,36]. Accordingly, different data interpretation approaches have been introduced to understand the creep behavior probed by the nanoindentation experiment [36,37]. We applied both the power-law and logarithmic-law approaches to fit the experimental results in this paper, but only achieved a good fit with the logarithmic function proposed by Vandamme & Ulm [36]. Thus the logarithmic-law approach was chosen in this paper and the fitting function is shown in Eq. (5).

$$\Delta L(t) = \frac{ln\left(\frac{t}{\tau} + 1\right)}{C} \tag{5}$$

where, C is the contact creep modulus and τ is a characteristic time. A large C value results in low creep compliance, that is, less creep strain. A large characteristic time τ indicates a slow creep rate [31,32].

Combining Eqs. (4) and (5), the change of indentation depth $\Delta h(t)$ has a logarithmic form with respect to the holding time:

$$\Delta h(t) = \alpha ln\left(\frac{t}{\tau} + 1\right) \tag{6}$$

$$\alpha = \frac{P_H}{2r_{cu}C}$$

However, a modified equation proposed by Vandamme [32] and Vandamme and Ulm [36] is used here to facilitate improved fitting with the experimental data:

$$\Delta h(t) = \alpha ln\left(\frac{t}{\tau} + 1\right) + \gamma t + \delta \tag{7}$$

The first term represents the logarithmic creep behavior of the material. The parameters α and τ characterize the creep properties as described above. The other terms and the corresponding parameters (γ and δ) only depend on the testing apparatus and fitting errors [20,31,36]. The contact creep modulus and the characteristic time of the geopolymer can be extracted by fitting Eq. (7) to the measured $\Delta h(t)$ curves (Fig. 3).

4. Results

4.1. Young's modulus and hardness

The extracted values of Young's modulus (E) and hardness (H) versus contact depth h_c are shown in Fig. 4. It can be seen that the inhomogeneity and polished-surface effect causes the extracted properties from 5 mN indentation to be quite scattered. As indentation load increased to 50 mN and beyond, the variation of the results reduced. This indicates that the influences of the inhomogeneity and polished-surface effect gradually reduce with the increasing probed volumes. As the indentation load increase (200 mN for mix1 and 400 mN for others), the extracted properties becomes stable and thus were taken as the representative value for different geopolymer compositions. By comparison, Mixes 2, 3, and 4 have a similar hardness (0.1 to 0.14 GPa) and Young's modulus (2.57 to 3.16 GPa). Mix 1 has the lowest hardness

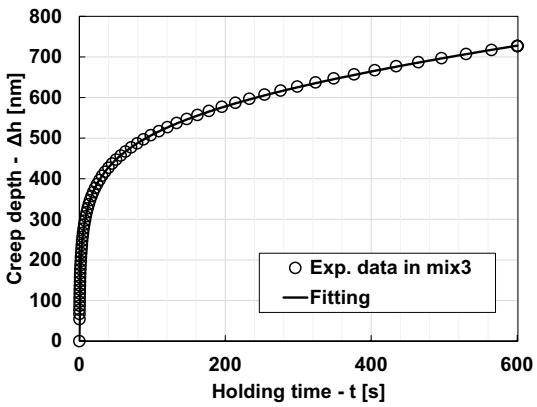

Fig. 3. Typical creep depth versus holding time response.

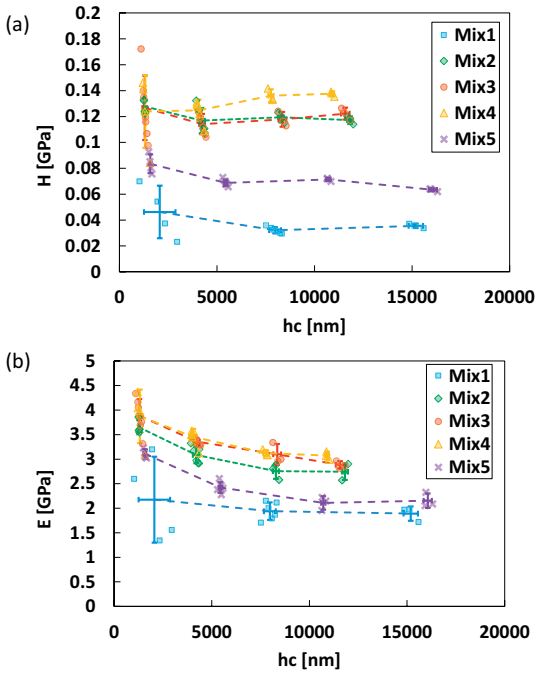

Fig. 4. Results of (a) hardness, (b) Young's modulus.

(0.033 to 0.037 GPa) and Young's modulus (1.72 to 1.97 GPa). Mix 5 has intermediate hardness (0.062 to 0.064 GPa) and Young's modulus (2.05 to 2.32 GPa). Compared with previous indentation studies on metakaolin-based geopolymers [39–41], the hardness and Young's modulus values measured here are relatively low compared to those reported by others (17 to 18 GPa by Němeček et al. [41] and 8.21 to 11.50 GPa by Pelisser et al. [40]). The hardness was reported to range from 0.17 to 0.42 GPa (Pelisser et al. [40]) and from 0.05 to 0.6 GPa (Subaer et al. [39]). The relatively lower measured Young's modulus and indentation hardness values primarily result from the higher water content (44.5%) compared with that in previous researches (approximately 22%-38% in Subaer et al. [39], 33%-35% in Pelisser et al. [40], and 38–39% in Němeček et al. [41]). Although the high water content decreased the absolute value of E and H, their trends with respect to chemical composition of the activator presented in our experiment are consistent with the findings of Pelisser et al. [40], which are that the excessively low silicate in the activator reduces the Young's modulus and hardness of the matrix. However, the reduced Young's modulus due to the high Si/Al ratio contradicts our previous findings from macroscale compressive tests, i.e., the Young's modulus was almost constant as the Si/Al ratio varied from 1.9 to 2.4 [30]. This deviation may be a result of the curing age of the sample. The relatively shorter curing age (14 d) in this study may have limited the reaction extent of the sample with the highest Si/Al ratio (Mix 5). Previous studies [42,43] had shown that the low pH value in high silicate-contained activators may retard the reaction of raw particles, and thus may need more curing time to achieve a close-to-full reaction. For other Si/Al ratios, however, the curing age is sufficient to produce a homogeneous matured gel with few unreacted raw materials, which was confirmed from the SEM images shown in the following sections. This phenomenon also indicates that the reaction rate of the geopolymer changes significantly for an Si/Al ratio ranging from 2.0 to 2.2. However, this delayed reaction effect may be relieved by extending the curing time.

4.2. Creep properties from nanoindentation

The indentation curves in the holding stage are shown in Fig. 5. The extracted creep properties based on the procedure described in Section 3 are shown in Fig. 6.

The contact-creep modulus at the highest load of Mixes 2, 3, and 4 with Si/Al ratio ranging from 1.6 to 2.0 are very similar (from 25 to 32 GPa). That of Mixes 1 and 5 with lower and higher Si/Al ratios, respectively, are approximately 50% lower than the former mixes (10 to 18 GPa). Variation in the creep modulus with respect to the Si/Al ratio exhibits a similar trend to the Young's modulus and hardness. The creep modulus is obviously reduced when the Si/Al ratio is excessively low or high. This trend indicates that the creep behavior in the geopolymer may be determined by the same structural factors that determine E and H, which will be discussed in later sections.

Moreover, compared with the results (40 to 105 GPa) extracted from fly-ash-based geopolymer samples with and without silicate fumes by Lee et al. [20] using a similar indentation method, the creep modulus in our samples is also relatively lower. As previously explained, this deviation can be partially attributed to the high water content in our samples. Another cause of the deviation may be the difference in holding force (5 mN to 400 mN in this research and 2 mN in Lee's). According to previous research [38], a higher holding force usually results in larger creep deformation and a low creep modulus. Our experiments show, however, that higher holding forces (above 50 mN) are needed in order to involve a sufficient volume (about tens of the characteristic pore size in length) to obtain a stable representative creep property of the binder.

On the other hand, the extracted characteristic times do not converge when the indentation load increases. As the indentation load increased, the characteristic times of different binders were also higher. For high indentation loads (200 mN and 400 mN), the differences in characteristic times of different binders became apparent. The binder with a lower hardness tended to have a lower characteristic time. This is reasonable because the weak materials usually need a lower activation energy in deformation. Thus, the external stress would accelerate the deformation process. Since the required activation energy of the material is low, the characteristic time is then shorter.

Similar to previous research [36], the parameter γ and δ in the fitting of the creep curves also showed little correlation with composition and mechanical properties (Fig. 7).

Data on geopolymer concretes reported in the literature [15,16,18,19] were compared with the test results from this study, as detailed in Appendix B. Although the raw materials, binder compositions and test details in these studies are different, these results could provide a comparison of the indentation creep test and bulk creep tests in geopolymer-based materials. The retreatment results are listed in Table 3. The results show that the contact creep modulus obtained from nanoindentation in this study (10 to 32 GPa) are lower than the creep modulus from the bulk uniaxial creep test in previous publications (20 to 60 GPa), but their magnitudes are still in the same order. By contrast, the characteristic times from the nanoindentation test (0.1 to 3.5 s) are significantly shorter than those shown in the bulk creep test (0.06 to 1.06 d). This short characteristic time is also shown in previous studies on contact creep behavior of OPCs [36] and fly ash based geopolymers [20] by nanoindentation. Considering that the probed volume is much smaller and the effective stress level is much higher in the indentation creep test, and thus, it is questionable to directly take the extracted binder scale creep properties as equivalents to that from conventional bulk scale creep tests without acknowledging these intrinsic differences. However, the indentation creep test could provide information about the composition dependency of the creep behaviors in a relatively short time. With calibrations with bulk scale results, this information may help the bulk scale rational design, but it is beyond the scope of this paper and will be investigated in future work.

4.3. Composition of the gel phase from EDS

As pointed out by Davidovits [1], the gel phase of the geopolymer is composed of three different aluminosilicate monomers, where alkali ions balance the negative charge of the aluminate center. Different Si/

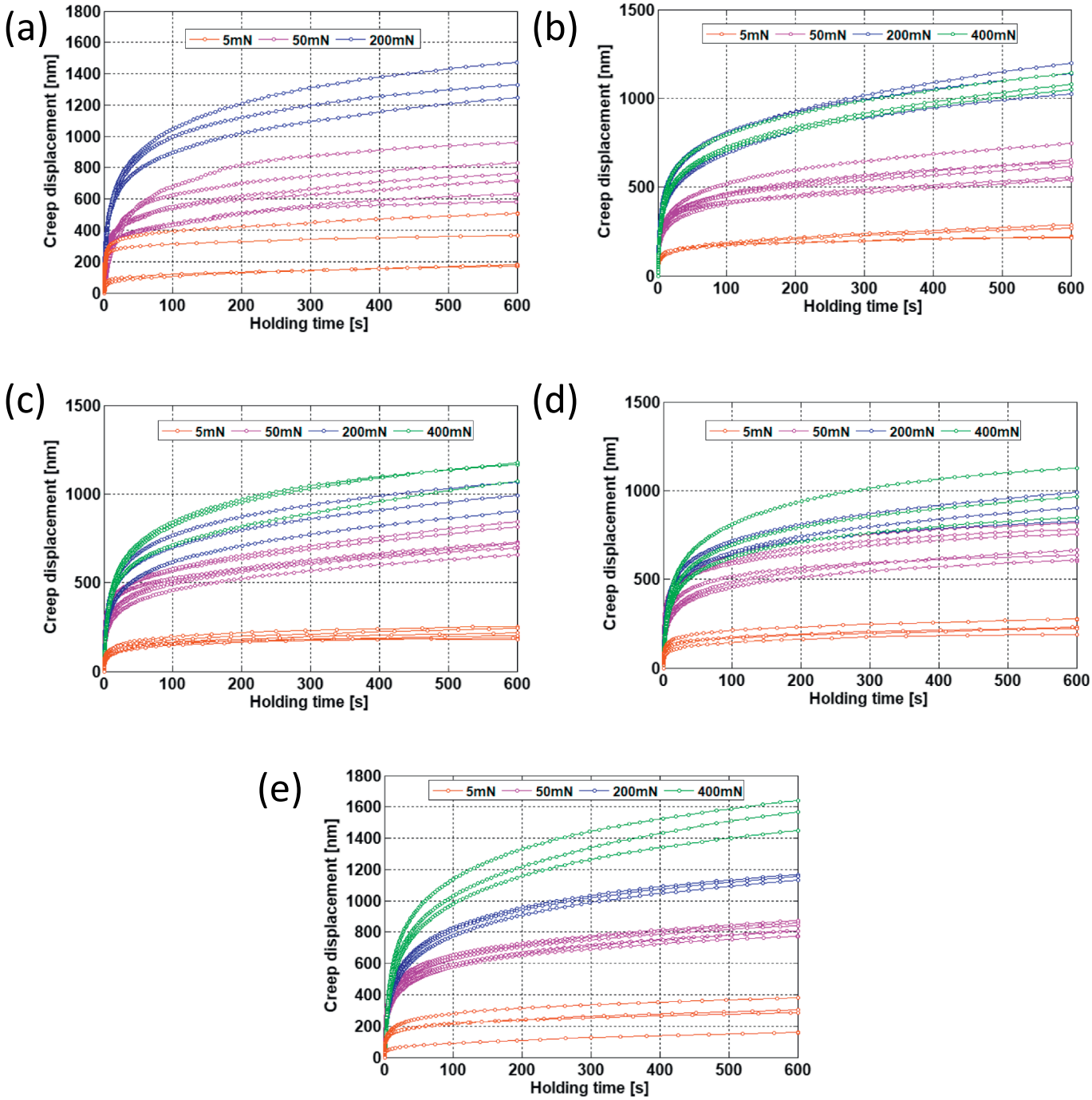

Fig. 5. Creep displacement versus holding time of (a) Mix1, (b) Mix2, (c) Mix3, (d) Mix4 and (e) Mix5.

Al ratios would result in different fractions of monomers and connecting coordinates in the aluminosilicate network [25]. In order to confirm whether the Si/Al ratio in the gel phase of the geopolymer in this experiment changed due to different initial Si/Al ratios in the mixture design, energy dispersive spectrometry (EDS) was used to identify the real elemental composition in hardened geopolymer binder samples. As shown in Fig. 8, the geopolymer matrix may contain different phases, such as the gel phase and unreacted MK particles. At locations where the gel phase occupied a major portion of the sample, the spectrum was collected and fitted to determine the relative atomic fraction of various elements. The Na/Al ratio and Si/Al ratio in each phase was calculated as follows:

$$\frac{\mathrm{Na}}{\mathrm{Al}} = \frac{\mathrm{At\%(Na)}}{\mathrm{At\%(Al)}} \tag{8}$$

$$\frac{\mathrm{Si}}{\mathrm{Al}} = \frac{\mathrm{At\%(Si)}}{\mathrm{At\%(Al)}} \tag{9}$$

where, At % (*) denotes the relative atomic (molar) fraction of a given element.

The chemical composition of the gel phase was determined statistically using data from 11 to 16 locations. The results show that the average Na/Al ratio of the gel phase ranges from 0.70 to 0.98 (Fig. 9(a)). These measured Na/Al ratios are relatively lower than the target value (1.0). This deviation may be caused by washing during polishing. Due to the fact that the reaction rate of the MK powder could

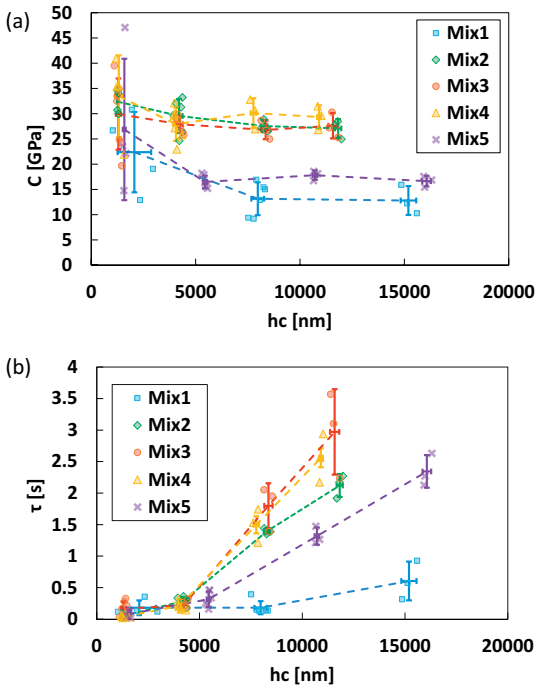

Fig. 6. Results of (a) creep modulus, (b) characteristic time.

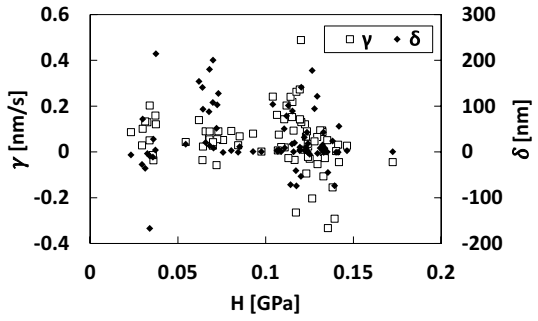

Fig. 7. Fitting parameter γ and δ versus the extracted hardness.

Table 3
Creep properties extracted from uniaxial creep test data reported in the literature.

Data source	Sample	σ [MPa]	C_{con} [GPa]	τ [d]	f_{agg}	C_{bin} [GPa]
Hardjito et al. (2004) [15]	A-2	22.00	562.37	0.06	0.77	60.02
Wallah (2010) [16]	1CR	27.00	508.47	0.13	0.77	54.27
	2CR	23.00	348.06	0.12	0.77	37.15
	3CR	19.00	227.68	0.52	0.77	24.30
	4CR	16.00	276.00	0.10	0.77	29.46
Islam (2015) [18]	GP4000	11.03	171.11	0.54	0.74	21.01
	GP8000	20.68	455.00	0.40	0.74	55.88
	GP35	14.07	316.57	0.50	0.74	38.88
	GP45	12.41	219.54	0.53	0.74	26.96
	GP55	11.03	168.17	0.30	0.74	20.65
	GP65	10.34	169.60	0.21	0.74	20.83
Castel et al.(2016) [19]	3D40	10.00	29.29	0.13	0.79	2.88
	7D80	20.00	434.88	1.06	0.79	42.71

not reach 100% and some calcium impurity was present in the MK powder, some sodium ions remain unbound in the framework of the N-A-S-H gel. As alkali ions are very leachable [44], they will dissolve out during washing with water, creating bias in the measurements. Compared with leachable alkali ions, the silicate and aluminate contents in the hardened geopolymer are more stable and difficult to dissolve. Thus, the measured Si/Al ratio is closer to the target value of the designed mixture, which could be seen in Fig. 9(b). This result provides a useful baseline for further analysis.

4.4. Gel morphology from SEM and XRD

The microstructure of geopolymer binders with different Si/Al ratios are shown in Fig. 10.

The gel phase in Mix 1, activated with the pure sodium hydroxide solution and with Si/Al ratio near 1.09, has a granular nature. Many cubic crystals are covered and bonded by smaller gel particles. From the EDS results (Fig. 11), the elemental composition of the crystal phase contains mostly O, Na, Al, and Si and with a Si/Al ratio near 1.1. The XRD results show that Mix 1 presents significant crystal peaks which belong to the zeolite-A phase. This feature was also reported in previous studies [27,39,45], where the Si/Al ratio of the composition ranged from 1.0 to 1.25. The elemental composition of the surrounding amorphous gel phase did not deviate significantly from the crystal phase. The amorphous phase exhibits slightly lower Na/Al ratio. This deviation may be primarily caused by the porous structure of the gel. The larger contact surface with the solutions in the pores helps unbound Na ions dissolve out, which further biases the measured composition. The crystal phase in Mix 1 increases the density of the skeletal matrix, but many large pores are also present in the surrounding gel phase.

The similar crystal phase is not present in the other geopolymer binders (Mixes 2, 3, 4, and 5), which were activated using the sodium silicate solution with Ms > 1.0. As shown in Fig. 12, the major XRD pattern in these mixtures are wide humps spread from 15° to 40° and centered at 27°-28°. Only peaks corresponding to quartz and anatase are present, which is primarily caused by crystal SiO_2 and TiO_2 impurities in the raw material. This hump pattern is featureless for different mixtures, except for a slight decrease in the center of the hump. This indicates that the matrix of the geopolymer with Si/Al ratio > 1.6 is primarily composed of the amorphous gel. Previous results from MK-based geopolymers with Si/Al ratio ranging from 1.5 to 4.0 also support this phase characterization [27]. The SEM images shown in Fig. 10(b)–(d) more clearly demonstrate that the major phases in these mixtures are homogeneous matured gels together with many micro or nano pores. The change in the Si/Al ratio did not significantly impose a structural change in the phase but rather differences in degrees of geopolymerization, as reported by He et al. [26]. Fig. 10(e) demonstrates that the matrix in Mix5 contains large residual metakaolin particles and the pores in the surrounding gel phase are larger in this mixture. But the major gel phase remains amorphous and contains no crystals which was shown in Mix1.

4.5. Pore structure from MIP

MIP measurements show that the pore structures in different mixtures could be more clearly distinguished. The results indicate that the porosity of the five different mixtures changes by very little (approximately 3% relative standard deviation) (Fig. 13(a)). Porosity derived from the MIP test ranges from 40.74% to 44.27%, with a mean value of 43%. There is no particular trend with respect to the Si/Al ratio. Similarly, the bulk density (including MIP pores) and skeletal density (excluding MIP pores) of samples are both irrelevant to the compositions (Fig. 13(b)). Therefore, it is rational to consider that the porosity of the sample did not vary greatly through different Si/Al ratios, although some very nano-sized pore volumes could not be characterized with MIP techniques. It is reasonable to attribute this minor difference in porosity to the constant water content in the designed composition. Pores form as water is removed from the matrix, and thus, a constant water content would result in constant porosity.

Conversely, the pore distribution in different mixtures has different

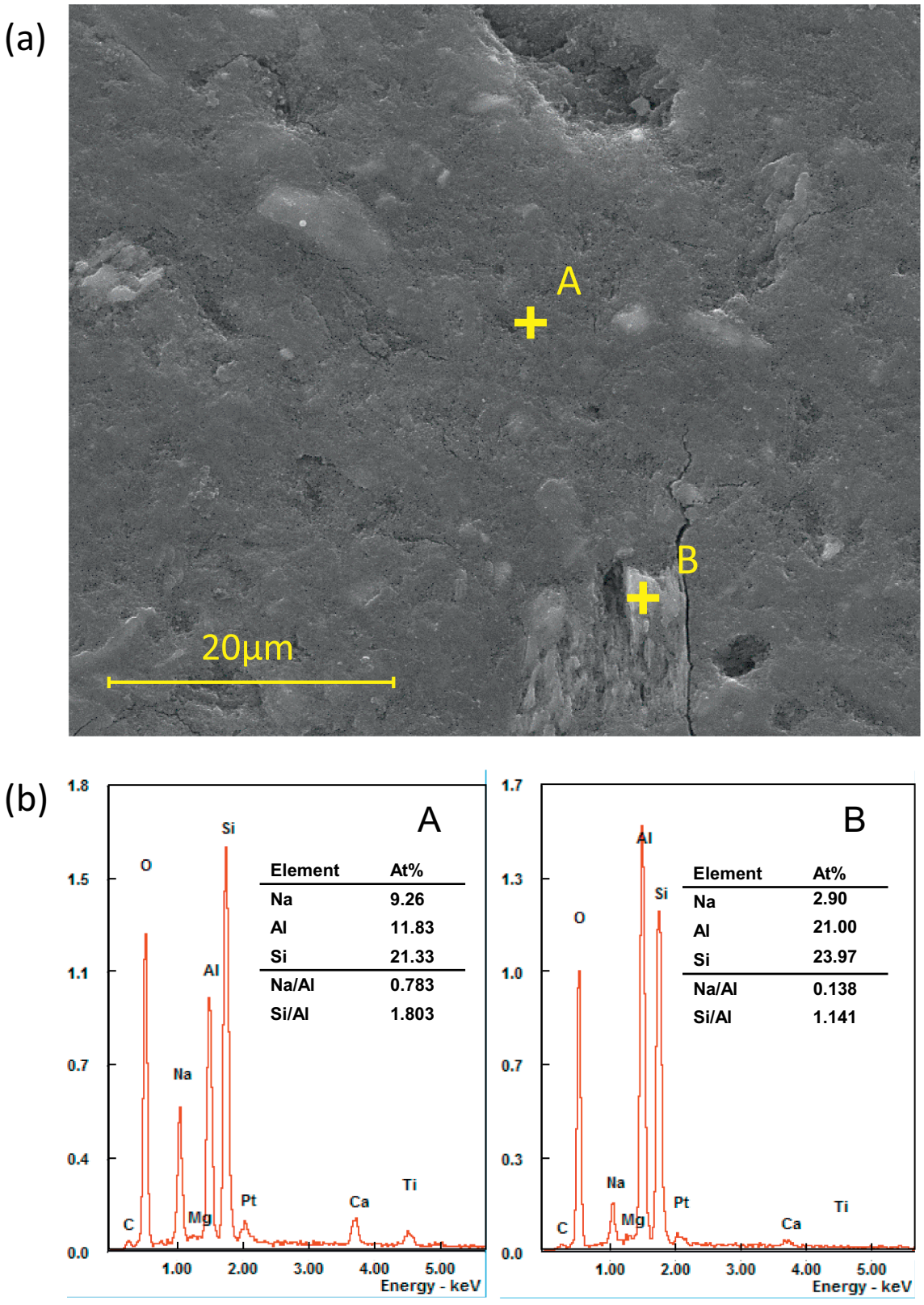

Fig. 8. (a) SEM and (b) EDS characterization of specimens with Mix3.

features. Fig. 14 shows that the characteristic pore size in Mix 1 is approximately 1300 nm, and its major pore distribution lays in the micro (several micrometers) and sub-micro (hundreds of nanometers) scales. At the same time, the characteristic pore sizes in Mixes 2, 3, and 4 are well below 50 nm and the sizes of major pores range from several to tens nanometers. Mix 5 has a slightly larger characteristic pore size (~100 nm), but the major pores are also distributed at the nanoscale.

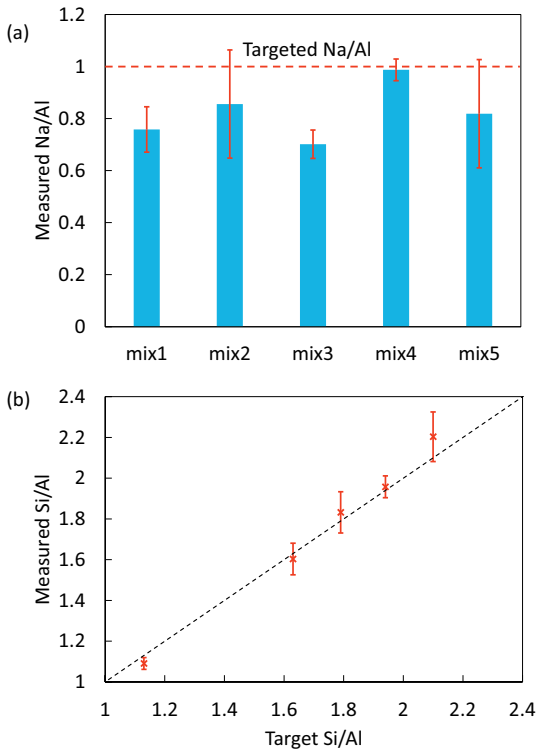

Fig. 9. The (a) Na/Al ratio and (b) Si/Al ratio measured by EDS analysis.

5. Discussion

5.1. Composition-dependent pore structure

Based on the previous microstructure characterizations, the gel phase morphology of geopolymer binders with different Si/Al ratios could be divided into three classes, as listed in Table 4. The most distinct feature of these three classes is the pore size distribution.

Fig. 15 shows a conceptual explanation of the influence of the Si/Al ratio on the pore structure.

As the Si/Al ratio approaches 1.0, the Ms of activator reaches zero. As a result, no external silicate was provided by the alkaline solution. Without soluble silicate in solution, all the silicate and aluminate species required to form a gel dissolve from the metakaolin particle. Moreover, with a low Si/Al ratio in gel composition, the granular crystal nuclei with sizes ranging from 3 to 5 μm are present within the gel. It leaves pores between them with sizes of similar order (several micrometers) (Fig. 15(a)). The formation of large pores due to the formation of zeolitic nuclei has also been reported in a previous publication [27].

When the Si/Al ratio increases, the amount of silicate species from the external activator increase. The gel would precipitate widelyand form a more homogeneous phase. Thus, the N-A-S-H gel with many nanopores and some residual distributed metakaolin particles forms the major phase in the binder. The micro pores between particles were largely removed (Fig. 15(b)).

When the Si/Al ratio is further increased, the silicate modulus of the alkali solution is then increased and the alkalinity of the solution would decrease with the formation of a large amount of silicate species [46],

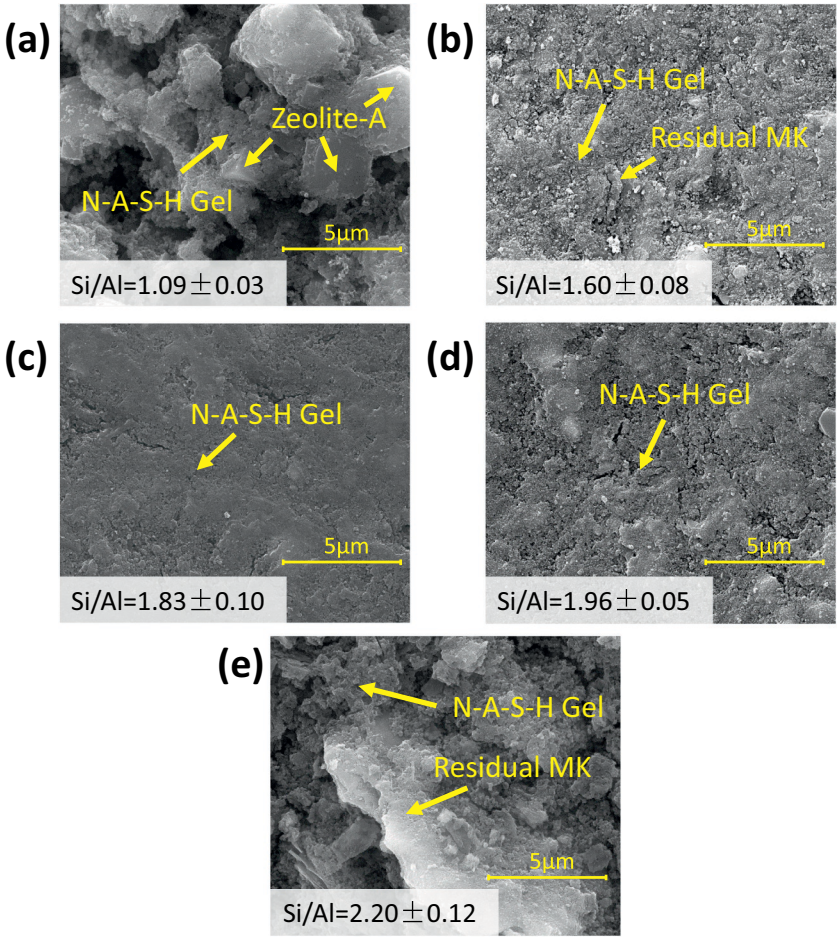

Fig. 10. Comparison of microstructure of (a) Mix1, (b) Mix2, (c) Mix3, (d) Mix4 and (e) Mix5.

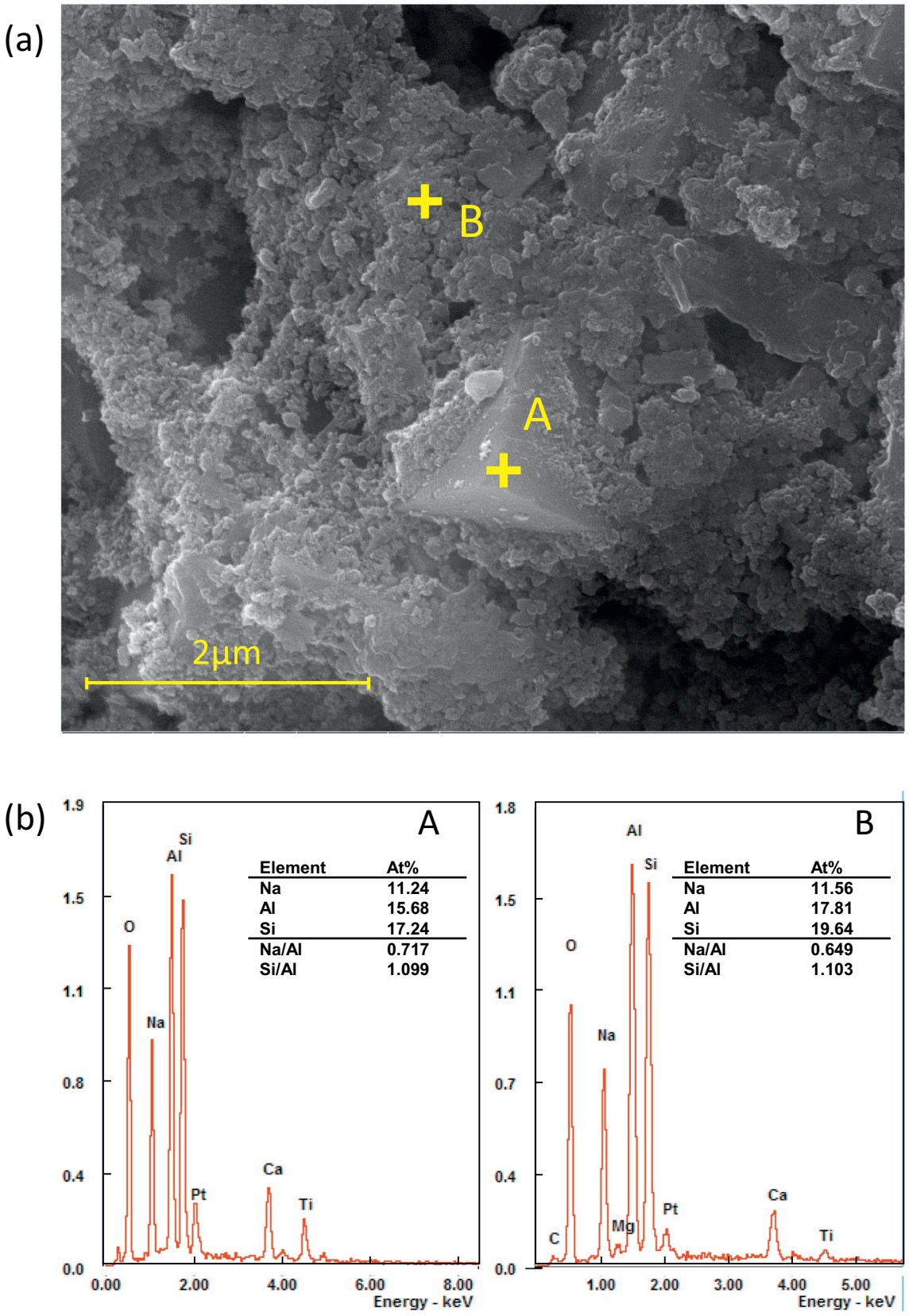

Fig. 11. (a) SEM and (b) EDS characterization of the crystal phase in mix1 sample.

which significantly affects the dissolution process of metakaolin particles. The extent of dissolution of raw material would decrease when the alkalinity decreased [47]. A portion of the large metakaolin particles would remain in the binder. The reduction in dissolved metakaolin results in the lack of aluminate species to form the gel. The void between the residual particles could not be fully filled by the gel and thus, some micro pores form (Fig. 15(c)).

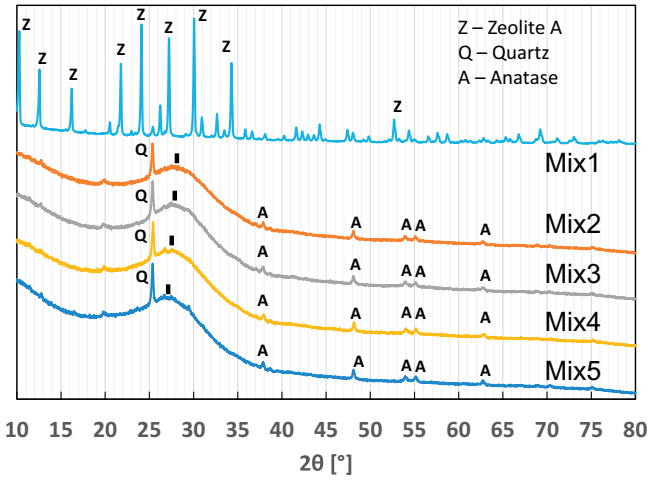

Fig. 12. XRD patterns.

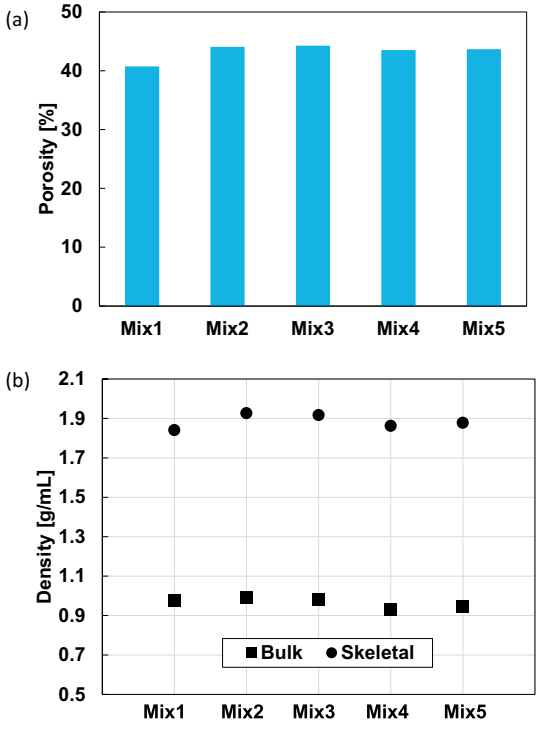

Fig. 13. (a) Porosity and (b) density of each mixture.

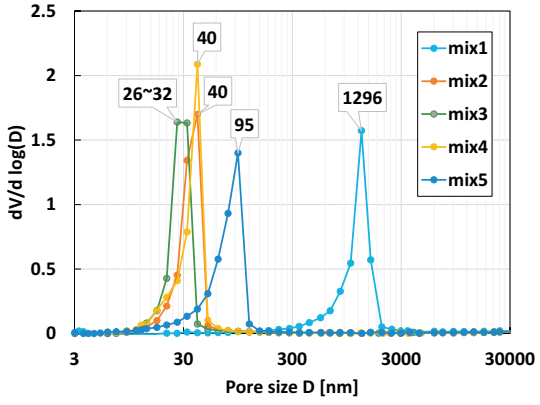

Fig. 14. The pore size distribution of each mixture.

Table 4
Classification of the gel phase morphologies.

Morphology	Si/Al	Structural order	Pore size
Class I	1.0–1.25	Crystal + amorphous	180–3500 nm
Class II	1.5–2.0	Amorphous	8–90 nm
Class III	> 2.1	Amorphous	10–180 nm

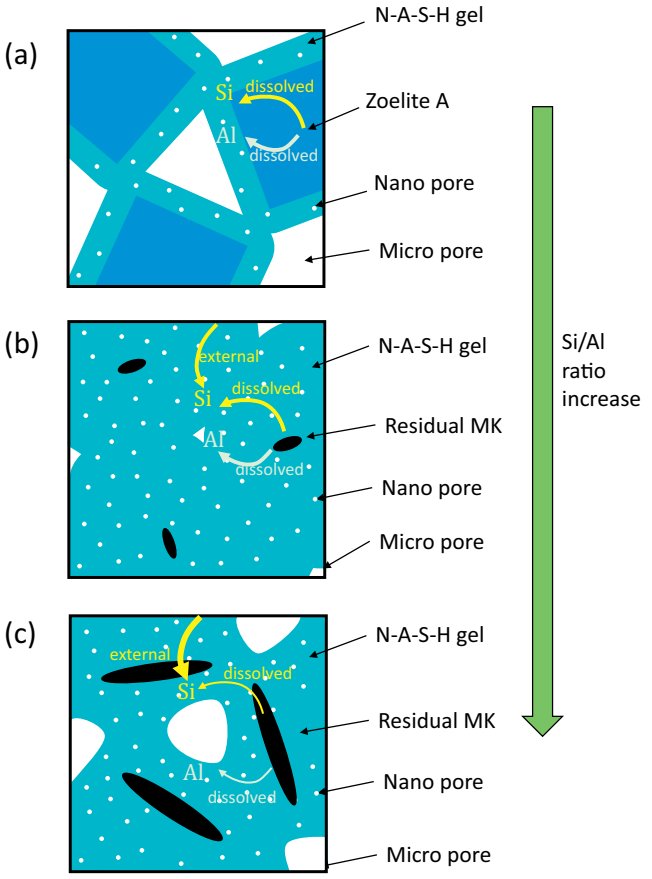

Fig. 15. Conceptual explanation of influence of Si/Al ratio on the pore structures.

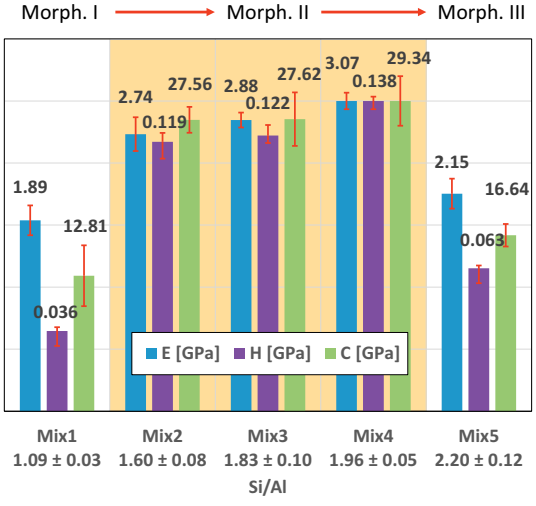

Fig. 16. Influence of the Si/Al ratio.

Table 5
Estimated properties of the inner matrix and surface layer.

	Thickness [nm]	Young's modulus [GPa]
Matrix	–	3.0–3.5
Surface layer	15–20	5.0–5.8

5.2. Correlation between pore structure and mechanical behavior

Fig. 16 demonstrates that divisions of the Si/Al ratio, based on mechanical properties extracted from the highest indentation load, coincide with the gel phase morphology classifications. When considering the MIP results, the major difference in the morphology of different mixes is the pore size distribution. The porosity (40.74% to 44.27%) is nearly the same for different mixes. Therefore, a pore size effect was observed from the nanoscale mechanical properties of MKG extracted from nanoindentation.

This pore size effect could be partially explained by a model of a "soft" porous solid with a "hard" pore surface layer. To quantitatively evaluate this pore size effect, a simple analytical model is introduced and detailed in Appendix C. The effective mechanical properties were evaluated by considering two-phase materials (matrix and surface layer around the pores) containing pores.

The estimated effective Young's modulus is shown in Table 5, and is congruent with the corresponding test results (± 1 std.) shown in Fig. 17. For comparison, the estimates without considering the surface layer are also shown in Fig. 17, and there is no dependence on pore size. This mechanism is very similar to that shown in surface-elasticity-induced size-effects in stiffness of the nanowires [48–50] and nanoporous materials [51,52]. Here, this trend was also found in the variation of hardness and creep modulus versus the characteristic pore size as shown in Fig. 18. Therefore, the surface layer structure present near the walls of the pores in MKG might not only influence the elastic behavior but also the yielding and viscous behaviors.

How these surface effect come from the structure of material is still an open question due to the lack of techniques to probe the material properties on the very surface. There is, however, evidence that the surface in sintered ceramics shows a different density to the inner cores [53], which may cause some surface effect. The existence of the surface layer in ambient-derived geopolymer at a scale of tens of nanometers is still not able to be proven in this paper. Furthermore, other explanations such as the intrinsic molecular structure changes [54] or the nanoscale interactions between gel network and confined water [55] would also contribute to the change in mechanical behaviors of MKG with different Si/Al ratios. This needs further studies which deep down to the molecular scale to thoroughly elucidate these fundamental mechanisms.

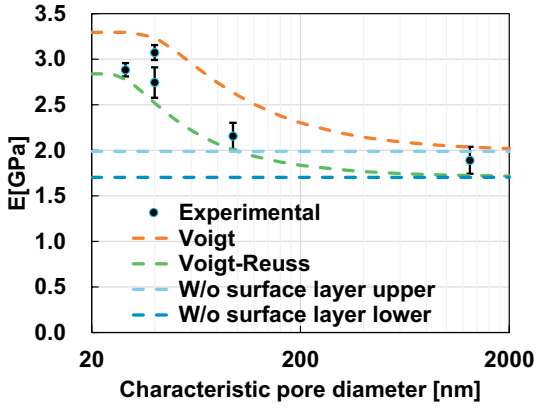

Fig. 17. Comparison between the model evaluation and the experimental results of Young's modulus.

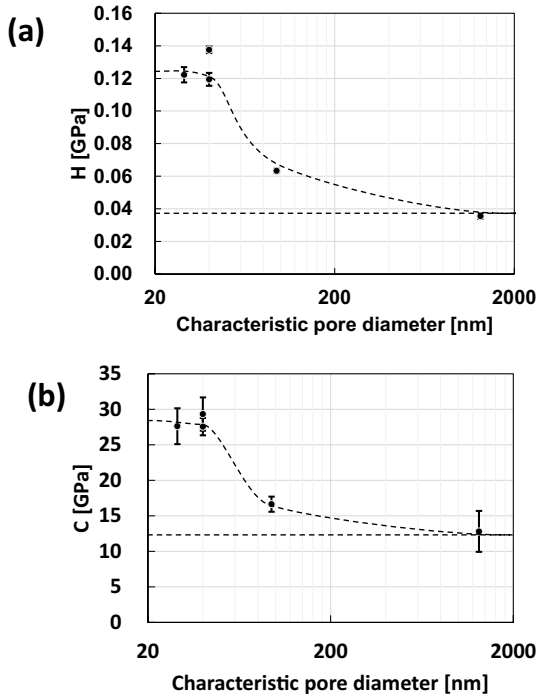

Fig. 18. Variation trend of (a) hardness and (b) creep modulus versus the characteristic pore diameter.

6. Conclusions

Our findings show that the creep modulus of geopolymer determined from nanoindentation measurements is found to be comparable to values measured with conventional macro-scale tests. However, the time required in nanoindentation is substantially lower. The Si/Al ratio has a significant influence on the microstructure and creep behavior in MKG, as well as on the Young's modulus and hardness. Its influence is largely attributed to modification of the microstructure of the binder, especially the major size of pores in the matrix according to the detailed analysis. When the average pore size decreases via optimization of the Si/Al ratio, the measured Young's modulus, hardness, and creep modulus increases, despite the nearly constant porosity. Moreover, a zeolitic phase was present when the Si/Al ratio approached 1.0, and large residual metakaolin particles were present when the Si/Al ratio approached 2.2. These microstructural changes led to an increased pore size of the binder and reduced Young's modulus, hardness, and creep modulus. When the Si/Al ratio ranged from 1.6 to 2.0, the MKG had pores majorly distributed over tens of nanometers with optimized mechanical properties. It could therefore be deducted that the pore size changes with varying Si/Al ratio may be related to the varying amount of silicate species and alkalinity of the alkaline activating solution, while the change of mechanical properties due to the pore size might be related to a surface layer around the pores based on micromechanical models and analysis. The existence of such structure is currently not able to be proven. Further studies are needed to thoroughly examine this mechanism and eliminate the results from other explanations.

Acknowledgement

This work is supported by National Key R&D Program of China (2018YFB0605700), National Natural Science Foundation of China (Nos. 51879230 and 51778570) and the Fundamental Research Funds for the Central University of China (No. 2019QNA4044). The Center for Infrastructure Engineering Studies at Missouri University of Science and Technology is also acknowledged for funding support. The authors would also appreciate the efforts of the anonymous reviewers to improve the quality of this study.

Appendix A

The indentation load versus displacement responses are shown in Fig. A1. Typical post-indentation sites are shown in Fig. A2. Based on the Oliver-Pharr method [29], the indentation modulus M can be calculated using the following equation:

$$M = \frac{1}{\frac{1}{E_r} - \frac{1}{M_i}} \tag{A1}$$

where, E_r is the effective modulus of the tested material and M_i is the indentation modulus of the indenter tip.

M_i is evaluated using Young's modulus (1141 GPa) and Poisson's ratio (0.07) of diamond [56] and with Eq. (1).

The effective modulus E_r is

$$E_r = \frac{\sqrt{\pi}}{2\beta}\frac{S}{\sqrt{A_c}} \tag{A2}$$

where, S is the elastic unloading stiffness, A_c is the contact area, and β is the correction coefficient that accounts for the shape of the tip. For the Berkovich tip used in this study, $\beta = 1.034$ as suggested by Oliver and Pharr [29].

The elastic unloading stiffness S could be evaluated from the unloading curve using Eq. (A3).

$$S = \frac{dP}{dh}\Big|_{h=h_m} \tag{A3}$$

where, h_m is the indentation depth during the initial unloading stage.

In this study, the value of S was estimated by fitting the initial 20% of the unloading curve to the linear function $P = c_1h + c_2$, where the slope of the fitted equation is $S = c_1$.

The contact area A_c was evaluated from the contact depth h_c. For the Berkovich tip used in this study, A_c and h_c are related as $A_c = 24.479\ h_c^2$ [57].

The contact depth h_c was evaluated using the Oliver-Pharr method:

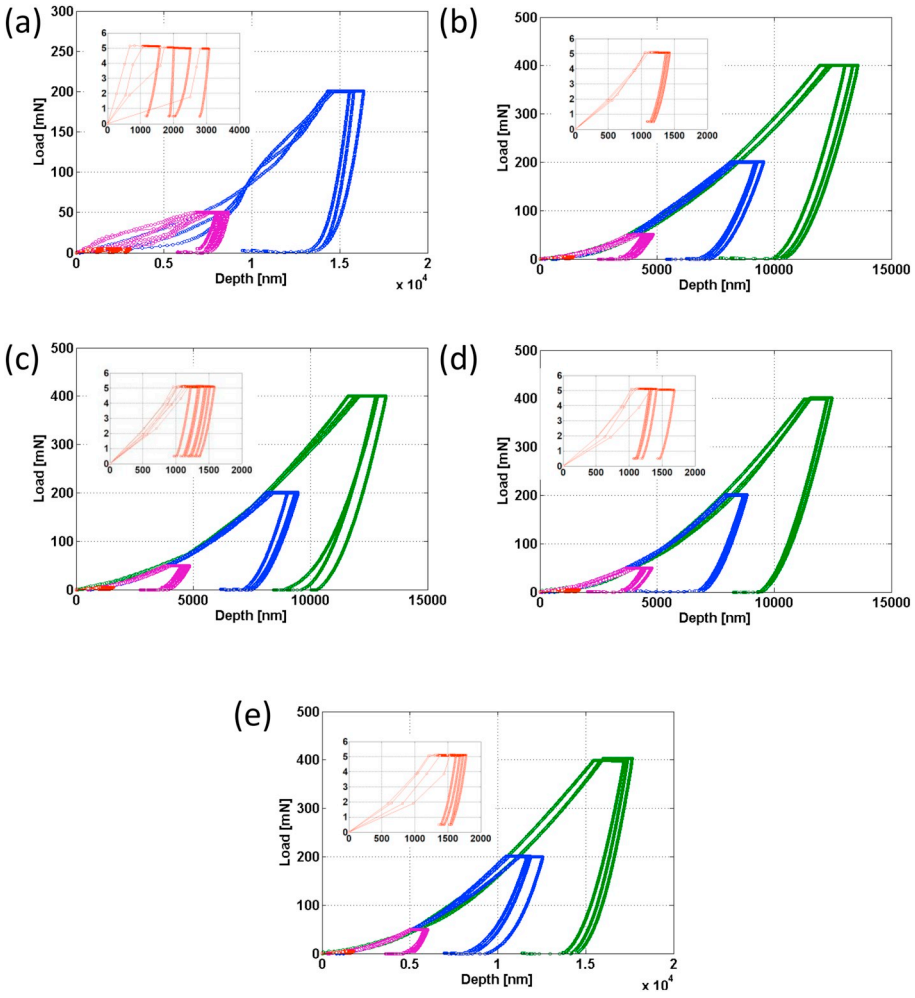

Fig. A1. Typical load-depth response of (a) Mix1, (b) Mix2, (c) Mix3, (d) Mix4, and (e) Mix5.

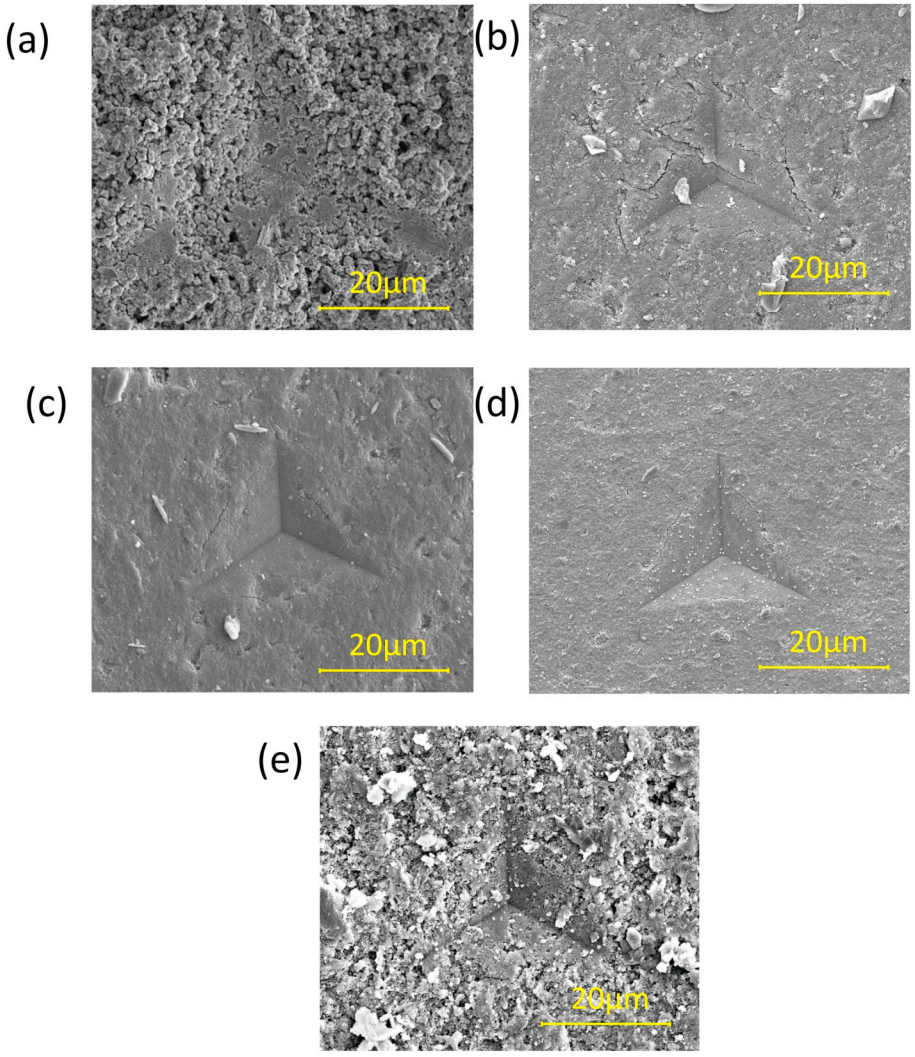

Fig. A2. Post-indentation (50mN) sites of (a) Mix1, (b) Mix2, (c) Mix3, (d) Mix4, and (e) Mix5.

$$h_c = h_m - \epsilon\frac{P_H}{S} \tag{A4}$$

where, h_m is the maximum indentation depth during the initial unloading and P_H is the holding force during the holding stage.

Appendix B

We can extract the creep modulus of the concrete materials using results from the uniaxial creep experiments

The basic creep compliance of a concrete material could be evaluated with

$$L(t) = \frac{\epsilon_{tot}(t) - \epsilon_s(t)}{\sigma} \tag{B1}$$

where, $\epsilon_{tot}(t)$ and $\epsilon_s(t)$ are the total strain measured under the sustained stress σ and the shrinkage strain measured without external loading during the test period, respectively.

The creep function, which is the difference between the elastic response and the basic creep compliance, is

$$\Delta L(t) = L(t) - \frac{1}{E_0} = \frac{\epsilon_{tot}(t) - \epsilon_s(t)}{\sigma} - \frac{\epsilon_e}{\sigma} = \frac{\Delta\epsilon(t)}{\sigma} \tag{B2}$$

$\Delta\epsilon(t) = \epsilon_{tot}(t) - \epsilon_s(t) - \epsilon_e$ is the strain increase purely due to creep and is usually given in the literature.

Following a similar method as the indentation creep, the creep strain increase during a uniaxial creep test could also be fitted to a logarithmic kinetics equation (Eq. (B3)):

$$\Delta\epsilon(t) = \alpha \ln\left(\frac{t}{\tau} + 1\right) \tag{B3}$$

The creep modulus of the concrete material is given by [31].

$$C_{con} = \frac{\sigma}{\alpha} \tag{B4}$$

and τ is the characteristic time.

As shown in previous studies [31,36], the creep modulus of the binder material could be further estimated from the creep modulus of the concrete material using a Mori–Tanaka scheme. In this homogenization, the creep of the matrix is considered to be deviatoric while the creep of the aggregate is ignored. Moreover, the adhesion between the binder and the aggregate is assumed to be perfect. This yields the estimation equation in (B5):

$$C_{bin} = \frac{2(1 - f_{agg})}{2 + 3f_{agg}} C_{con} \tag{B5}$$

where, f_{agg} is the volume fraction of the aggregate.

Appendix C

The mechanical behavior of a porous solid with randomly distributed pores and surface layers (Fig. C1(a)) was simply modeled as a regular foam with orthogonal pore network and surrounding surface layers (Fig. C1(b)). For simplicity, the pore section was considered as a square with dimension d, and the thickness of the surface layer t was considered constant (if it does not exceed the limit $d + 2t < l$). A unit cell in the regular foam is shown in Fig. C1(c). The size of the cell l, pore dimension d, and the porosity ϕ_p obey the following relationship

$$\phi_p = 3\left(\frac{d}{l}\right)^2 - 2\left(\frac{d}{l}\right)^3 \tag{C1}$$

The ratio $\frac{d}{l} = 0.456$ if $\phi_p = 0.43$. The volume fraction of the solid matrix could also be calculated using the following:

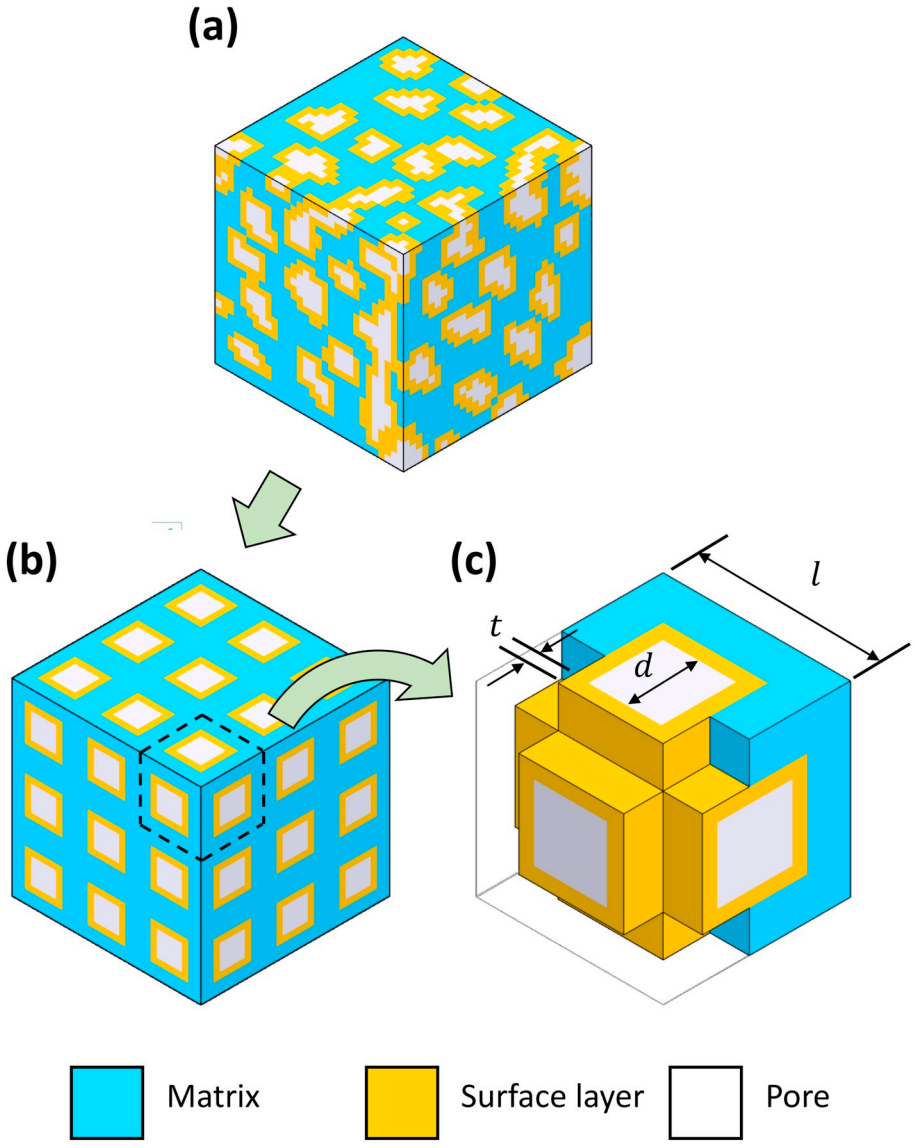

Fig. C1. Schematic of modeling (a) random porous solid with pore size effect with, (b) regular foam with orthogonal square pore network and surrounding surface layers (c) unit cell of the regular foam model. (For clarity, the near half of the matrix is removed to show the inner structures).

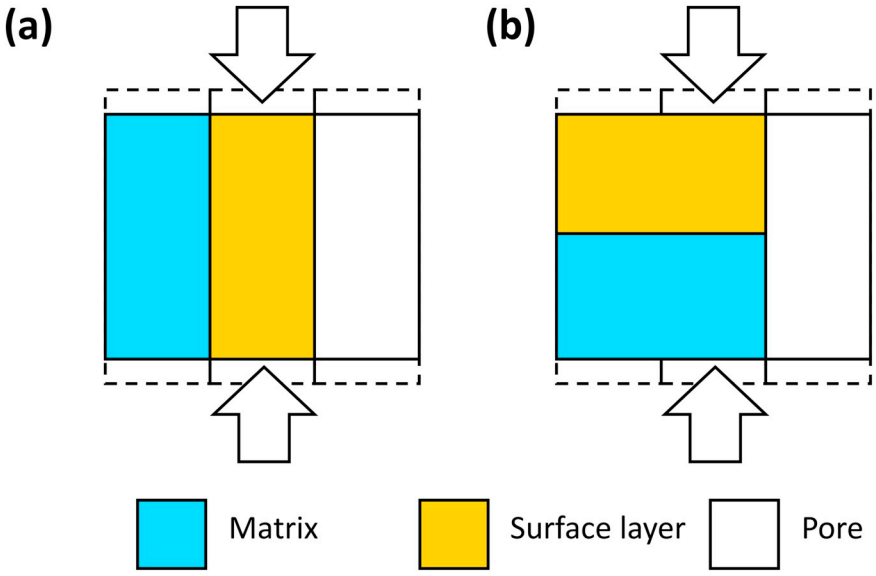

Fig. C2. Schematics of mixture law based on (a) Voigt, and (b) mixed Voigt-Reuss method.

$$\phi_m = \left\{3\left(1-\frac{d}{l}-2\frac{t}{l}\right)^2\left(\frac{d}{l}+2\frac{t}{l}\right)+\left(1-\frac{d}{l}-2\frac{t}{l}\right)^3,\ d+2t<l, 0,\ d+2t\geq l\right. \tag{C2}$$

The volume fraction of the surface layer is:

$$\phi_s = 1-\phi_p-\phi_m \tag{C3}$$

When the thickness of surface layer t exceeds the limit $d + 2t < l$, the foam would only be composed as a harder phase and pores, thus $\phi_s = 1 - \phi_p$.

The effective mechanical properties could be estimated using the simple mixture law [58]. The Voigt method (Fig. C2(a)), which considers components bearing the same strain, provides an upper bound on the effective properties:

$$E_{eff} = E_m\phi_m + E_s\phi_s \tag{C4}$$

where, E_{eff}, E_m, and E_s are the Young's modulus of the regular foam, the matrix, and the surface layer, respectively. The contribution from the pore is neglected.

At the same time, a mixed Voigt-Reuss method (Fig. C2(b)), which considers solid components (matrix and surface layer) bearing the same stress while the void (pores) sustains no stress and experiences the same deformation, then provides a lower bound on the effective properties:

$$E_{eff} = (1-\phi_p)\left(\left(\frac{1}{\phi_s+\phi_m}\right)\left(\frac{\phi_s}{E_s}+\frac{\phi_m}{E_m}\right)\right)^{-1} \tag{C5}$$

The properties of the matrix and surface layer could be roughly estimated by comparing the upper and lower bound of the effective properties obtained using Eqs. (C4) and (C5) with the experimental results.

References

[1] J. Davidovits, Geopolymers, J. Therm. Anal. Calorim. 37 (1991) 1633–1656.
[2] P. Duxson, J.L. Provis, G.C. Lukey, J.S.J. van Deventer, The role of inorganic polymer technology in the development of “green concrete”, Cem. Concr. Res. 37 (2007) 1590–1597, https://doi.org/10.1016/j.cemconres.2007.08.018.
[3] J.L. Provis, Geopolymers and other alkali activated materials: why, how, and what? Mater. Struct. Constr. 47 (2014) 11–25, https://doi.org/10.1617/s11527-013-0211-5.
[4] F.G. Collins, L.K. Turner, Carbon dioxide equivalent (CO2-e) emissions: a comparison between geopolymer and OPC cement concrete, Constr. Build. Mater. 43 (2013) 125–130, https://doi.org/10.1016/J.CONBUILDMAT.2013.01.023.
[5] G. Habert, C. Ouellet-Plamondon, Recent update on the environmental impact of geopolymers, RILEM Tech. Lett. 1 (2016) 17, https://doi.org/10.21809/rilemtechlett.v1.6.
[6] P. Duan, C. Yan, W. Zhou, W. Luo, C. Shen, An investigation of the microstructure and durability of a fluidized bed fly ash metakaolin geopolymer after heat and acid exposure, Mater. Des. 74 (2015) 125–137.
[7] M.A.M. Ariffin, M.A.R. Bhutta, M.W. Hussin, M. Mohd Tahir, N. Aziah, Sulfuric acid resistance of blended ash geopolymer concrete, Constr. Build. Mater. 43 (2013) 80–86, https://doi.org/10.1016/j.conbuildmat.2013.01.018.
[8] A. Fernández-Jiménez, J.Y. Pastor, A. Martín, A. Palomo, High-temperature resistance in alkali-activated cement, J. Am. Ceram. Soc. 93 (2010) 3411–3417, https://doi.org/10.1111/j.1551-2916.2010.03887.x.
[9] W.D.A. Rickard, G.J.G. Gluth, K. Pistol, In-situ thermo-mechanical testing of fly ash geopolymer concretes made with quartz and expanded clay aggregates, Cem. Concr. Res. 80 (2016) 33–43, https://doi.org/10.1016/j.cemconres.2015.11.006.
[10] Z.P. Bazant, L. Panula, Creep and shrinkage characterization for analysing prestressed concrete structures, PCI J. 25 (1980) 86–122.
[11] V. Sicard, R. Francois, E. Ringot, G. Pons, Influence of creep and shrinkage on cracking in high strength concrete, Cem. Concr. Res. 22 (1992) 159–168, https://doi.org/10.1016/0008-8846(92)90146-M.
[12] Z.P. Bažant, Prediction of concrete creep and shrinkage: past, present and future, Nucl. Eng. Des. 203 (2001) 27–38, https://doi.org/10.1016/S0029-5493(00)00299-5.
[13] F. Barpi, S. Valente, Creep and fracture in concrete: a fractional order rate approach, Eng. Fract. Mech. 70 (2003) 611–623, https://doi.org/10.1016/S0013-7944(02)00041-3.
[14] F. Benboudjema, F. Meftah, J.M. Torrenti, Interaction between drying, shrinkage, creep and cracking phenomena in concrete, Eng. Struct. 27 (2005) 239–250, https://doi.org/10.1016/j.engstruct.2004.09.012.
[15] D. Hardjito, S.E. Wallah, D.M.J. Sumajouw, B.V. Rangan, On the development of fly ash-based geopolymer concrete, ACI Mater. J. 101 (2004) 467–472, https://doi.org/10.14359/13485.
[16] S.E. Wallah, Creep behaviour of fly ash-based geopolymer concrete, Civ. Eng. Dimens. 12 (2010), https://doi.org/10.9744/ced.12.2.73-78.
[17] K. Sagoe-Crentsil, T. Brown, A. Taylor, Drying shrinkage and creep performance of geopolymer concrete, J. Sustain. Cem. Mater. 2 (2013) 35–42, https://doi.org/10.1080/21650373.2013.764963.

[18] M.R. Islam, Louisiana Tech University (Ed.), Creep and Shrinkage Behavior of Fly Ash Based Geopolymer Concrete, 2015.

[19] A. Castel, S.J. Foster, T. Ng, J.G. Sanjayan, R.I. Gilbert, Creep and drying shrinkage of a blended slag and low calcium fly ash geopolymer concrete, Mater. Struct. Constr. 49 (2016) 1619–1628, https://doi.org/10.1617/s11527-015-0599-1.

[20] H. Lee, V. Vimonsatit, P. Chindaprasirt, T. Ngo, P. Mendis, Creep properties of cement and alkali activated fly ash materials using nanoindentation technique, Constr. Build. Mater. 168 (2018) 547–555, https://doi.org/10.1016/j.conbuildmat.2018.02.166.

[21] S.E. Wallah, B.V. Rangan, Low-Calcium Fly Ash-Based Geopolymer Concrete: Long-Term Properties, (2006), https://doi.org/10.1017/CBO9781107415324.004.

[22] N.P. Lee, Creep and Shrinkage of Inorganic Polymer Concrete, Judgeford, New Zealand, 2007.

[23] P. Duxson, S.W. Mallicoat, G.C. Lukey, W.M. Kriven, J.S.J. van Deventer, The effect of alkali and Si/Al ratio on the development of mechanical properties of metakaolin-based geopolymers, Colloids Surf. A Physicochem. Eng. Asp. 292 (2007) 8–20, https://doi.org/10.1016/j.colsurfa.2006.05.044.

[24] Matthew Rowles, Brian O'Connor, Chemical optimisation of the compressive strength of aluminosilicate geopolymers synthesised by sodium silicate activation of metakaolinite, J. Mater. Chem. 13 (2003) 1161–1165, https://doi.org/10.1039/b212629j.

[25] C.E. White, J.L. Provis, T. Proffen, J.S.J. van Deventer, Molecular mechanisms responsible for the structural changes occurring during geopolymerization: multiscale simulation, AICHE J. 58 (2012) 2241–2253, https://doi.org/10.1002/aic.12743.

[26] P. He, M. Wang, S. Fu, D. Jia, S. Yan, J. Yuan, J. Xu, P. Wang, Y. Zhou, Effects of Si/Al ratio on the structure and properties of metakaolin based geopolymer, Ceram. Int. 42 (2016) 14416–14422, https://doi.org/10.1016/j.ceramint.2016.06.033.

[27] Q. Wan, F. Rao, S. Song, R.E. García, R.M. Estrella, C.L. Patiño, Y. Zhang, Geopolymerization reaction, microstructure and simulation of metakaolin-based geopolymers at extended Si/Al ratios, Cem. Concr. Compos. 79 (2017) 45–52, https://doi.org/10.1016/j.cemconcomp.2017.01.014.

[28] S. El-Safty, N. Silikas, R. Akhtar, D.C. Watts, Nanoindentation creep versus bulk compressive creep of dental resin-composites, Dent. Mater. 28 (2012) 1171–1182, https://doi.org/10.1016/j.dental.2012.08.012.

[29] G.M. Pharr, W.C. Oliver, Measurement of hardness and elastic modulus by instrumented indentation: advances in understanding and refinements to methodology, J. Mater. Res. 19 (2004) 3–20, https://doi.org/10.1557/jmr.2004.19.1.3.

[30] D. Yan, S. Chen, Q. Zeng, S. Xu, H. Li, Correlating the elastic properties of metakaolin-based geopolymer with its composition, Mater. Des. 95 (2016) 306–318, https://doi.org/10.1016/j.matdes.2016.01.107.

[31] Q. Zhang, R. Le Roy, M. Vandamme, B. Zuber, Long-term creep properties of cementitious materials: comparing microindentation testing with macroscopic uniaxial compressive testing, Cem. Concr. Res. 58 (2014) 89–98, https://doi.org/10.1016/j.cemconres.2014.01.004.

[32] M. Vandamme, The Nanogranular Origin of Concrete Creep: A Nanoindentation Investigation of Microstructure and Fundamental Properties of Calcium-Silicate-Hydrates, (2008).

[33] M. Königsberger, M. Irfan-ul-Hassan, B. Pichler, C. Hellmich, Downscaling based identification of nonaging power-law creep of cement hydrates, J. Eng. Mech. 142 (2016) 04016106, , https://doi.org/10.1061/(asce)em.1943-7889.0001169.

[34] B.T. Tamtsia, J.J. Beaudoin, Basic creep of hardened cement paste. A re-examination of the role of water, Cem. Concr. Res. 30 (2000) 1465–1475, https://doi.org/10.1016/S0008-8846(00)00279-9.

[35] M. Irfan-ul-Hassan, M. Königsberger, R. Reihsner, C. Hellmich, B. Pichler, How water-aggregate interactions affect concrete creep: multiscale analysis, J. Nanomechanics Micromechanics. 7 (2017) 04017019, , https://doi.org/10.1061/(asce)nm.2153-5477.0000135.

[36] M. Vandamme, F.J. Ulm, Nanoindentation investigation of creep properties of calcium silicate hydrates, Cem. Concr. Res. 52 (2013) 38–52, https://doi.org/10.1016/j.cemconres.2013.05.006.

[37] C.A. Jones, Z.C. Grasley, Short-term creep of cement paste during nanoindentation, Cem. Concr. Compos. 33 (2011) 12–18, https://doi.org/10.1016/j.cemconcomp.2010.09.016.

[38] J. Nemecek, Creep effects in nanoindentation of hydrated phases of cement pastes, Mater. Charact. 60 (2009) 1028–1034, https://doi.org/10.1016/j.matchar.2009.04.008.

[39] A.H. Subaer, A.I. Nurhayati, J.J. Ekaputri, The influence of Si:Al and Na:Al on the physical and microstructure characters of Geopolymers based on Metakaolin, Mater. Sci. Forum 841 (2016) 170–177, https://doi.org/10.4028/www.scientific.net/MSF.841.170.

[40] F. Pelisser, E.L. Guerrino, M. Menger, M.D. Michel, J.A. Labrincha, Micromechanical characterization of metakaolin-based geopolymers, Constr. Build. Mater. 49 (2013) 547–553, https://doi.org/10.1016/j.conbuildmat.2013.08.081.

[41] J. Němeček, V. Šmilauer, L. Kopecký, Nanoindentation characteristics of alkali-activated aluminosilicate materials, Cem. Concr. Compos. 33 (2011) 163–170, https://doi.org/10.1016/j.cemconcomp.2010.10.005.

[42] K. Sagoe-Crentsil, L. Weng, Dissolution processes, hydrolysis and condensation reactions during geopolymer synthesis: part II. High Si/Al ratio systems, J. Mater. Sci. 42 (2007) 3007–3014, https://doi.org/10.1007/s10853-006-0818-9.

[43] P.S. Singh, M. Trigg, I. Burgar, T. Bastow, Geopolymer formation processes at room temperature studied by 29Si and 27Al MAS-NMR, Mater. Sci. Eng. A 396 (2005) 392–402.

[44] Z. Aly, E.R. Vance, D.S. Perera, Aqueous dissolution of sodium aluminosilicate geopolymers derived from metakaolin, J. Nucl. Mater. 424 (2012) 164–170, https://doi.org/10.1016/j.jnucmat.2012.02.027.

[45] I. Ozer, S. Soyer-Uzun, Relations between the structural characteristics and compressive strength in metakaolin based geopolymers with different molar Si/Al ratios, Ceram. Int. 41 (2015) 10192–10198, https://doi.org/10.1016/j.ceramint.2015.04.125.

[46] J.L. Provis, P. Duxson, G.C. Lukey, F. Separovic, W.M. Kriven, J.S.J. Van Deventer, Modeling speciation in highly concentrated alkaline silicate solutions, Ind. Eng. Chem. Res. 44 (2005) 8899–8908, https://doi.org/10.1021/ie050700i.

[47] Y.K. Cho, S.W. Yoo, S.H. Jung, K.M. Lee, S.J. Kwon, Effect of Na2O content, SiO2/Na2O molar ratio, and curing conditions on the compressive strength of FA-based geopolymer, Constr. Build. Mater. 145 (2017) 253–260, https://doi.org/10.1016/j.conbuildmat.2017.04.004.

[48] S. Cuenot, C. Frétigny, S. Demoustier-Champagne, B. Nysten, Surface tension effect on the mechanical properties of nanomaterials measured by atomic force microscopy, Phys. Rev. B - Condens. Matter Mater. Phys. 69 (2004), https://doi.org/10.1103/PhysRevB.69.165410.

[49] C.Q. Chen, Y. Shi, Y.S. Zhang, J. Zhu, Y.J. Yan, Size dependence of Young's modulus in ZnO nanowires, Phys. Rev. Lett. 96 (2006), https://doi.org/10.1103/PhysRevLett.96.075505.

[50] E.C.C.M. Silva, L. Tong, S. Yip, K.J. Van Vliet, Size effects on the stiffness of silica nanowires, Small 2 (2006) 239–243, https://doi.org/10.1002/smll.200500311.

[51] A. Mathur, J. Erlebacher, Size dependence of effective Young's modulus of nanoporous gold, Appl. Phys. Lett. 90 (2007), https://doi.org/10.1063/1.2436718.

[52] X.Q. Feng, R. Xia, X. Li, B. Li, Surface effects on the elastic modulus of nanoporous materials, Appl. Phys. Lett. 94 (2009), https://doi.org/10.1063/1.3067999.

[53] R. German, Sintering: From Empirical Observations to Scientific Principles, (2014), https://doi.org/10.1016/C2012-0-00717-X.

[54] F. Lolli, H. Manzano, J.L. Provis, M.C. Bignozzi, E. Masoero, Atomistic simulations of Geopolymer models: the impact of disorder on structure and mechanics, ACS Appl. Mater. Interfaces 10 (2018) 22809–22820, https://doi.org/10.1021/acsami.8b03873.

[55] M.R. Sadat, S. Bringuier, A. Asaduzzaman, K. Muralidharan, L. Zhang, A molecular dynamics study of the role of molecular water on the structure and mechanics of amorphous geopolymer binders, J. Chem. Phys. 145 (2016), https://doi.org/10.1063/1.4964301.

[56] A.C. Fischer-Cripps, Critical review of analysis and interpretation of nanoindentation test data, Surf. Coat. Technol. 200 (2006) 4153–4165, https://doi.org/10.1016/j.surfcoat.2005.03.018.

[57] C. Jin, D.M. Ebenstein, Nanoindentation of compliant materials using Berkovich tips and flat tips, J. Mater. Res. 32 (2017) 435–450, https://doi.org/10.1557/jmr.2016.483.

[58] C.J. Haecker, E.J. Garboczi, J.W. Bullard, R.B. Bohn, Z. Sun, S.P. Shah, T. Voigt, Modeling the linear elastic properties of Portland cement paste, Cem. Concr. Res. 35 (2005) 1948–1960, https://doi.org/10.1016/j.cemconres.2005.05.001.